

WWZ/ γ production in the large extra dimensions model at the LHC and ILC

Li Xiao-Zhou, Duan Peng-Fei, Ma Wen-Gan, Zhang Ren-You, and Guo Lei
*Department of Modern Physics, University of Science and Technology of China (USTC),
 Hefei, Anhui 230026, People's Republic of China*
 (Received 27 August 2012; published 5 November 2012)

We investigate the effect induced by the Kaluza-Klein (KK) graviton in the $W^+W^- \gamma/Z$ production in the framework of the large extra dimensions (LED) model at both the CERN Large Hadron Collider (LHC) and the International Linear Collider (ILC). The integrated cross sections and various kinematic distributions in the LED model are presented and compared with those in the standard model. The results show that the contributions from KK-graviton exchange remarkably affect the observables of the triple gauge boson ($W^+W^- \gamma/Z$) production processes at both the ILC and LHC, particularly either in the high transverse momentum region or in the central rapidity region. We also find that the relative LED discrepancy for the $W^+W^- \gamma/Z$ production at the LHC is generally larger than that at the ILC due to the additional LED contribution via gg fusion subprocess and the KK-graviton exchanging resonant effect induced by the continuous large colliding energy in pp collision. We conclude that the $W^+W^- \gamma$ and W^+W^-Z productions at the LHC could have the distinct advantage over at the ILC from the aspect of effectively exploring the LED signal in measuring $W^+W^- \gamma/Z$ production.

DOI: [10.1103/PhysRevD.86.095008](https://doi.org/10.1103/PhysRevD.86.095008)

PACS numbers: 11.10.Kk, 14.70.Fm, 14.70.Hp

I. INTRODUCTION

The CERN Large Hadron Collider (LHC) and the upcoming International Linear Collider (ILC) are expected to perform precision tests of the standard model (SM) and explore the new physics at the TeV scale [1]. The large extra dimensions (LED) model is one of the scenarios beyond the SM that are proposed to solve the hierarchy problem [2]. The LED model has only one fundamental scale, $M_S \sim \text{TeV}$, and it may induce predictable collider phenomena at both the LHC and ILC. Up to now, many works on both the virtual Kaluza-Klein (KK) graviton exchange and the real KK-graviton production have been presented; for example, the $e^+e^- \rightarrow VV$ and $pp \rightarrow VV, VG, G + \text{jet}$ processes were studied in the LED model in Refs. [3–7].

In fact, the triple gauge boson (TGB) production processes are sensitive to the quartic gauge couplings (QGCs) and thus related to the electroweak symmetry breaking mechanism [8]. Any deviation from the SM prediction hints at the existence of new physics, such as the Higgsless or extra dimension signals [8,9]. In discriminating physics beyond the SM, we should investigate the potential contributions from the extension models. Compared with the thoroughly studied diboson production processes in extra dimension models, the TGB productions have been fully studied in the SM [10] but gained less attention in the LED model. Not long ago, the neutral TGB production processes at the LHC, $pp \rightarrow \gamma\gamma\gamma$, $pp \rightarrow \gamma\gamma Z$, $pp \rightarrow \gamma ZZ$, and $pp \rightarrow ZZZ$ were studied in the framework of the LED model in Ref. [11].

In this paper, we investigate the possible contributions of the virtual KK-graviton exchange to the $W^+W^- \gamma$ and W^+W^-Z productions at both the LHC and ILC. The

motivation for this work is shown in two fields: Firstly, the $W^+W^- \gamma$ and W^+W^-Z processes are directly related to the SM QGCs, namely $W^+W^- \gamma\gamma$, $W^+W^- \gamma Z$, and $W^+W^- ZZ$, which are different from the absence of the neutral QGCs in the SM at the tree level [11]. Secondly, although the experimental precision is limited by our understanding of strong QCD background, the LHC can provide more precision measurements of the QGCs than the existing data from the LEP II and Tevatron searches due to its very high energy and luminosity [12,13]. Furthermore, in the future, the QGCs can be further probed with higher precision at the ILC due to its cleaner environment [14]. In this sense, the LHC and the upcoming ILC will provide complementary studies on the TGB production channels. The paper is organized as follows: In Sec. II, we present the related theory of the LED model used in our calculations. In Sec. III, the calculation strategies are presented. The numerical results and analyses for the $W^+W^- \gamma$ and W^+W^-Z production processes at both colliders are provided in Sec. IV, and a short summary is given in the last section.

II. RELATED THEORY

In the LED model [2], the spacetime is $D = 4 + n$ with n being the number of extra dimensions. The only fundamental scale M_S unifying the gravity and the gauge interactions is at the TeV. To explore the phenomenological effects, one can extract the low-energy effective theory by the KK reduction in the brane-bulk picture [2,15]. In this scenario, the SM particles are confined on a $(3 + 1)$ -dimensional brane world volume while the gravity can propagate in the D -dimensional bulk. After the assumed torus compactification of the extra dimensions n , the usual

Planck scale M_P in the $(3+1)$ spacetime is related to the fundamental scale M_S as $M_P^2 \sim R^n M_S^{n+2}$ [16], where R is the radius of the n torus.

In the following calculations, we adopt the de Donder gauge for the KK-graviton part, while the Feynman gauge ($\xi = 1$) is used for the SM part. We assume all the momenta flow to the vertices, except that the fermionic momenta are set to be along with the fermion flow directions. Then we list the Feynman rules for the relevant vertices and the propagator of spin-2 KK graviton in the LED model below [15], where $G_{\text{KK}}^{\mu\nu}$, ψ , $W^{\pm\mu}$, Z^μ , and A^μ represent the fields of the graviton, fermion, W boson, Z boson, and photon, respectively:

(i) $G_{\text{KK}}^{\mu\nu}(k_3) - \bar{\psi}(k_1) - \psi(k_2)$ vertex:

$$-i\frac{\kappa}{8}[\gamma^\mu(k_1+k_2)^\nu + \gamma^\nu(k_1+k_2)^\mu - 2\eta^{\mu\nu}(k_1+k_2 - 2m_\psi)], \quad (2.1)$$

(ii) $G_{\text{KK}}^{\mu\nu}(k_4) - \bar{\psi}(k_1) - \psi(k_2) - A^\rho(k_3)$ vertex:

$$ieQ_f\frac{\kappa}{4}(\gamma^\mu\eta^{\nu\rho} + \gamma^\nu\eta^{\mu\rho} - 2\gamma^\rho\eta^{\mu\nu}), \quad (2.2)$$

(iii) $G_{\text{KK}}^{\mu\nu}(k_4) - \bar{\psi}(k_1) - \psi(k_2) - Z^\rho(k_3)$ vertex:

$$-ie\frac{\kappa}{4}[(\gamma^\mu\eta^{\nu\rho} + \gamma^\nu\eta^{\mu\rho} - 2\gamma^\rho\eta^{\mu\nu})(v_f - a_f\gamma_5)], \quad (2.3)$$

(iv) $G_{\text{KK}}^{\mu\nu}(k_3) - W^{+\rho}(k_1) - W^{-\sigma}(k_2)$ vertex:

$$-i\kappa\left[B^{\mu\nu\rho\sigma}m_W^2 + (C^{\mu\nu\rho\sigma\tau\beta} - C^{\mu\nu\rho\beta\sigma\tau})k_{1\tau}k_{2\beta} + \frac{1}{\xi}E^{\mu\nu\rho\sigma}(k_1, k_2)\right], \quad (2.4)$$

(v) $G_{\text{KK}}^{\mu\nu}(k_4) - W^{+\rho}(k_1) - W^{-\sigma}(k_2) - A^\lambda(k_3)$ vertex:

$$-ie\kappa[(k_1 - k_3)_\tau C^{\mu\nu\tau\sigma\rho\lambda} + (k_2 - k_1)_\tau C^{\mu\nu\sigma\rho\tau\lambda} + (k_3 - k_2)_\tau C^{\mu\nu\lambda\sigma\tau\rho}], \quad (2.5)$$

(vi) $G_{\text{KK}}^{\mu\nu}(k_4) - W^{+\rho}(k_1) - W^{-\sigma}(k_2) - Z^\lambda(k_3)$ vertex:

$$ie\frac{s_w}{c_w}\kappa[(k_1 - k_3)_\tau C^{\mu\nu\tau\sigma\rho\lambda} + (k_2 - k_1)_\tau C^{\mu\nu\sigma\rho\tau\lambda} + (k_3 - k_2)_\tau C^{\mu\nu\lambda\sigma\tau\rho}], \quad (2.6)$$

where $e = \sqrt{4\pi\alpha}$, α is the fine-structure constant, Q_f is the electric charge of fermion, $s_w(c_w)$ are sine (cosine) of the Weinberg angle, the vector and axial vector couplings of the Z boson; i.e., v_f and a_f are the same as in the SM, and $\kappa = \sqrt{16\pi}G_N$ is related to the reduced Planck mass as

$\bar{M}_P = \sqrt{2}\kappa^{-1}$, where G_N is the Newton constant. The tensor coefficients $B^{\mu\nu\alpha\beta}$, $C^{\rho\sigma\mu\nu\alpha\beta}$, and $E^{\mu\nu\rho\sigma}(k_1, k_2)$ are expressed as [6]

$$\begin{aligned} B^{\mu\nu\alpha\beta} &= \frac{1}{2}(\eta^{\mu\nu}\eta^{\alpha\beta} - \eta^{\mu\alpha}\eta^{\nu\beta} - \eta^{\mu\beta}\eta^{\nu\alpha}), \\ C^{\rho\sigma\mu\nu\alpha\beta} &= \frac{1}{2}[\eta^{\rho\sigma}\eta^{\mu\nu}\eta^{\alpha\beta} - (\eta^{\rho\mu}\eta^{\sigma\nu}\eta^{\alpha\beta} \\ &\quad + \eta^{\rho\nu}\eta^{\sigma\mu}\eta^{\alpha\beta} + \eta^{\rho\alpha}\eta^{\sigma\beta}\eta^{\mu\nu} \\ &\quad + \eta^{\rho\beta}\eta^{\sigma\alpha}\eta^{\mu\nu})], \\ E^{\mu\nu\rho\sigma}(k_1, k_2) &= \eta^{\mu\nu}(k_1^\rho k_1^\sigma + k_2^\rho k_2^\sigma + k_1^\rho k_2^\sigma) \\ &\quad - [\eta^{\nu\sigma}k_1^\mu k_1^\rho + \eta^{\nu\rho}k_2^\mu k_2^\sigma + (\mu \leftrightarrow \nu)]. \end{aligned}$$

After summation over KK states, the spin-2 KK-graviton propagator can be expressed as [6]

$$\tilde{G}_{\text{KK}}^{\mu\nu\alpha\beta} = \frac{1}{2}D(s)\left[\eta^{\mu\alpha}\eta^{\nu\beta} + \eta^{\mu\beta}\eta^{\nu\alpha} - \frac{2}{n+2}\eta^{\mu\nu}\eta^{\alpha\beta}\right], \quad (2.7)$$

where

$$D(s) = \frac{16\pi}{\kappa^2} \frac{s^{n/2-1}}{M_S^{n+2}} [\pi + 2iI(\Lambda/\sqrt{s})], \quad (2.8)$$

and

$$I(\Lambda/\sqrt{s}) = P \int_0^{\Lambda/\sqrt{s}} dy \frac{y^{n-1}}{1-y^2}. \quad (2.9)$$

The integral $I(\Lambda/\sqrt{s})$ contains an ultraviolet cutoff Λ on the KK modes [15,16]. It should be understood that the point $y = 1$ has been removed from the integration path, and we set the ultraviolet cutoff Λ to be the fundamental scale M_S routinely. The real part proportional to π in Eq. (2.8) is from the narrow resonant production of a single KK mode with $m_n^2 = s$, and the imaginary part $I(M_S/\sqrt{s})$ is from the summation over the many nonresonant states.

III. CALCULATIONS

The $W^+W^-\gamma$ and W^+W^-Z productions at the LHC arise from the quark-antiquark annihilation and the gluon-gluon fusion subprocesses at the parton level:

$$q(p_1) + \bar{q}(p_2) \rightarrow W^+(p_3) + W^-(p_4) + V(p_5), \quad (3.1)$$

$$(q = u, d, s, c, b),$$

$$g(p_1) + g(p_2) \rightarrow W^+(p_3) + W^-(p_4) + V(p_5). \quad (3.2)$$

The $e^+e^- \rightarrow W^+W^-\gamma$, W^+W^-Z processes at the ILC can be denoted as

$$e^+(p_1) + e^-(p_2) \rightarrow W^+(p_3) + W^-(p_4) + V(p_5). \quad (3.3)$$

In reactions (3.1), (3.2), and (3.3), $V = \gamma, Z$, and p_i ($i = 1, 2, 3, 4, 5$) represent the four-momenta of initial and final

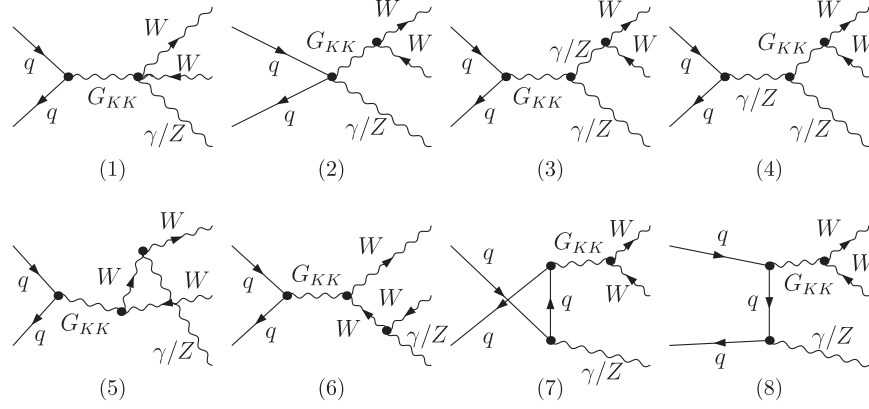


FIG. 1. The LO Feynman diagrams for the partonic process $q\bar{q} \rightarrow W^+W^-\gamma/Z$ with KK-graviton exchange in the LED model. The SM-like diagrams are not shown.

particles. The leading order (LO) Feynman diagrams with KK-graviton exchange for the (3.1) and (3.2) channels are shown in Figs. 1 and 2, respectively, while the LO additional Feynman diagrams in the LED model for the process (3.3) are depicted in Fig. 3.

From these Feynman diagrams, one can find that the KK graviton couples not only to the fermion pair, vector boson pair, and fermion-antifermion-vector boson ($f\bar{f}VG_{KK}$), but also to the TGB including charged gauge boson, which is absent in the neutral TGB production processes as shown in Ref. [11]. Therefore, it is natural to expect that KK graviton in the LED model may induce considerable effects at the TeV scale on the TGB production processes concerning charged gauge bosons at the LHC and the future ILC.

We express the Feynman amplitudes for the partonic processes $q\bar{q} \rightarrow W^+W^-\gamma/Z$ and $gg \rightarrow W^+W^-\gamma/Z$ as

$$\begin{aligned} \mathcal{M}_{q\bar{q}}^{\gamma/Z} &= \mathcal{M}_{q\bar{q}}^{\gamma/Z,SM} + \mathcal{M}_{q\bar{q}}^{\gamma/Z,LED}, \\ \mathcal{M}_{gg}^{\gamma/Z} &= \mathcal{M}_{gg}^{\gamma/Z,LED}, \end{aligned} \quad (3.4)$$

where $\mathcal{M}_{q\bar{q}}^{\gamma/Z,SM}$ ($q = u, d, c, s, b$) is the amplitude contributed by the SM-like diagrams, while $\mathcal{M}_{q\bar{q}}^{\gamma/Z,LED}$ and $\mathcal{M}_{gg}^{\gamma/Z,LED}$ are the amplitudes with KK-graviton exchange. The Feynman amplitude for the $e^+e^- \rightarrow W^+W^-\gamma/Z$ process can be expressed as

$$\mathcal{M}_{ee}^{\gamma/Z} = \mathcal{M}_{ee}^{\gamma/Z,SM} + \mathcal{M}_{ee}^{\gamma/Z,LED}, \quad (3.5)$$

where $\mathcal{M}_{ee}^{\gamma/Z,SM}$ stands for the amplitude mediated by the SM-like particles, while $\mathcal{M}_{ee}^{\gamma/Z,LED}$ is mediated by the KK graviton.

The total cross sections for the partonic process $q\bar{q}(gg) \rightarrow W^+W^-\gamma/Z$ can be expressed as

$$\begin{aligned} \hat{\sigma}_{ij}^{\gamma/Z} &= \frac{1}{4|\vec{p}|\sqrt{s}} \int d\Gamma_3 \sum'_{spin} \sum'_{color} |\mathcal{M}_{ij}^{\gamma/Z}|^2, \\ (ij &= u\bar{u}, d\bar{d}, c\bar{c}, s\bar{s}, b\bar{b}, gg), \end{aligned} \quad (3.6)$$

where \vec{p} is the three-momentum of one initial parton in the center-of-mass system (c.m.s.), the summation is taken over the spins or colors of initial and final particles, the prime on the sum recalls averaging over initial spins or colors, and $d\Gamma_3$ is the three-body phase space element expressed as

$$d\Gamma_3 = (2\pi)^4 \delta^{(4)}\left(p_1 + p_2 - \sum_{i=3}^5 p_i\right) \prod_{i=3}^5 \frac{d^3\vec{p}_i}{(2\pi)^3 2E_i}. \quad (3.7)$$

By convoluting $\hat{\sigma}_{ij}^{\gamma/Z}$ with the parton distribution functions (PDFs) of the colliding protons, the total cross section for the $pp \rightarrow W^+W^-\gamma/Z$ parent process can be written as

$$\begin{aligned} \sigma_{pp}^{\gamma/Z} &= \sum_{ij=u\bar{u}, d\bar{d}, s\bar{s}}^{c\bar{c}, b\bar{b}, gg} \frac{1}{1 + \delta_{ij}} \int dx_A dx_B [G_{i/A}(x_A, \mu_f) \\ &\times G_{j/B}(x_B, \mu_f) \hat{\sigma}_{ij}^{\gamma/Z}(\sqrt{s} = x_A x_B \sqrt{s}) + (A \leftrightarrow B)], \end{aligned} \quad (3.8)$$

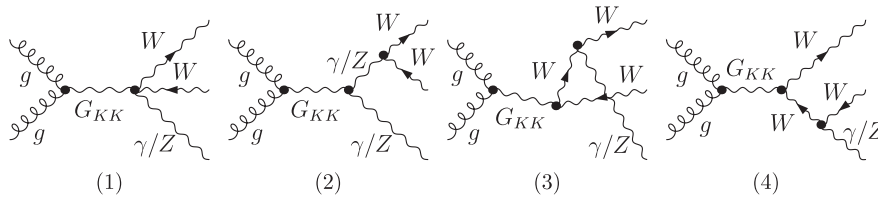


FIG. 2. The LO Feynman diagrams for the gluon-gluon fusion subprocess $gg \rightarrow W^+W^-\gamma/Z$ with KK-graviton exchange in the LED model.

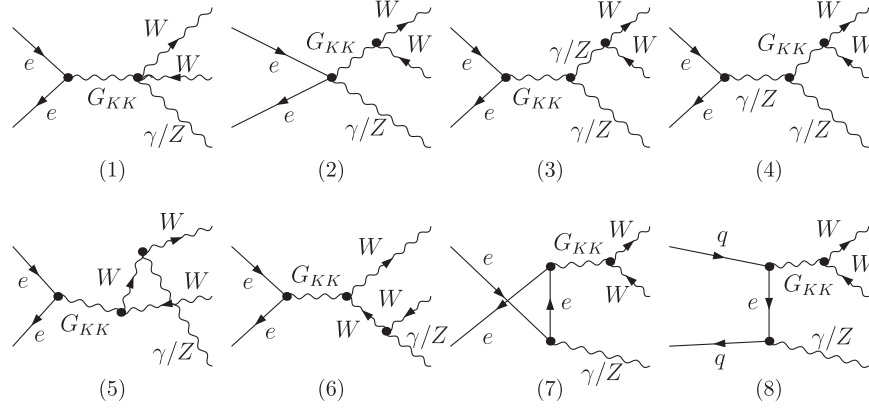


FIG. 3. The LO Feynman diagrams for the $e^+e^- \rightarrow W^+W^-\gamma/Z$ process with KK-graviton exchange in the LED model. The SM-like diagrams are not shown.

where $G_{i/P}$ ($i = q, \bar{q}, g$) represents the PDF of parton i in proton $P (= A, B)$, μ_f is the factorization scale, and x_A and x_B describe the momentum fractions of parton (quark or gluon) in protons A and B , respectively. The expression for the total cross section for $e^+e^- \rightarrow W^+W^-\gamma/Z$ is

$$\sigma_{ee}^{\gamma/Z} = \frac{1}{4|\vec{p}|\sqrt{s}} \int d\Gamma_3 \sum_{\text{spin}} |\mathcal{M}_{ee}^{\gamma/Z}|^2, \quad (3.9)$$

where \vec{p} is the three-momentum of the incoming e^+ (or e^-) in the c.m.s. of the e^+e^- collider. The prime on the sum means averaging over initial spin states as declared for Eq. (3.6).

IV. NUMERICAL RESULTS AND DISCUSSIONS

In this section, we present the numerical results in both the SM and the LED model at the LHC and ILC. For the calculations at the LHC, we use the CTEQ6L1 PDFs [17] with $\Lambda_{\text{QCD}} = 165$ MeV and $n_f = 5$; the factorization scale is set to be $\mu_f = m_W$ and $\mu_f = m_W + m_Z/2$ for the $pp \rightarrow W^+W^-\gamma$ and $pp \rightarrow W^+W^-Z$ processes, respectively. The active quarks are taken as massless; i.e., $m_q = 0$, ($q = u, d, c, s, b$), the CKM matrix is set to be the unit matrix. The other related input parameters are taken as [18]

$$\begin{aligned} \alpha^{-1}(0) &= 137.036, & m_W &= 80.385 \text{ GeV}, \\ m_Z &= 91.1876 \text{ GeV}, & M_H &= 125 \text{ GeV}, \\ m_t &= 173.5 \text{ GeV}, & m_e &= 0.511 \times 10^{-3} \text{ GeV}. \end{aligned} \quad (4.1)$$

Since the LED model is an effective low-energy theory, it breaks down in the nonperturbative region where $\sqrt{s}(\sqrt{\hat{s}}) \simeq M_S$ or above. In order to make reliable and viable phenomenological predictions, we take the hard and conservative truncation scheme as setting the cut $\sqrt{\hat{s}} < M_S$ for proton-proton collision and the limit $\sqrt{s} \sim 1 \text{ TeV} < M_S$ for the e^+e^- collision, where $\sqrt{\hat{s}}$ and \sqrt{s} are the partonic and e^+e^- c.m.s. energies, respectively. In evaluating the $e^+e^-/pp \rightarrow W^+W^-\gamma$ processes, we put a transverse

momentum cut $p_T^\gamma > 25 \text{ GeV}$ and a rapidity cut $|\eta^\gamma| < 2.7$ on the final photon in order to get rid of the IR singularity at the tree level.

Recently, the LED parameters M_S and n have obtained more severe constraints by the LHC experiments. The ATLAS Collaboration provided 95% confidence level lower limits on M_S in the range of 2.27–3.53 TeV depending on the number of extra dimensions n in the range of 7 to 3 [19]. The diphoton searches at CMS set $2.3 \text{ TeV} < M_S < 3.8 \text{ TeV}$ [20], and the dilepton experiments at CMS set the limit on M_S as $2.5 \text{ TeV} < M_S < 3.8 \text{ TeV}$ with the number of extra dimensions n varying from 7 to 3 at 95% confidence level [21]. In our calculations we take $M_S = 3.8 \text{ TeV}$ and $n = 3$ unless otherwise stated.

For the verification of the correctness of our numerical calculations, we use both the FeynArts 3.5 [22] and CompHEP 4.5.1 [23] packages to calculate the integrated cross sections for the $e^+e^- \rightarrow W^+W^-\gamma/Z$ and $pp \rightarrow W^+W^-\gamma/Z$ processes at the $\sqrt{s} = 800 \text{ GeV}$ ILC and the $\sqrt{s} = 14 \text{ TeV}$ LHC in the SM separately. We take the input parameters, PDFs, and the event selection criteria as mentioned above. The numerical results are listed in Table I. It demonstrates that the results from the two packages are in good agreement within the calculation errors.

We present the transverse momentum (p_T) distributions of final W^- boson, γ , and Z boson for the $e^+e^- \rightarrow W^+W^-\gamma, W^+W^-Z$ processes at the $\sqrt{s} = 800 \text{ GeV}$ ILC

TABLE I. The integrated cross sections for the processes $e^+e^- \rightarrow W^+W^-\gamma/Z$ and $pp \rightarrow W^+W^-\gamma/Z$ in the SM at the $\sqrt{s} = 800 \text{ GeV}$ ILC and the $\sqrt{s} = 14 \text{ TeV}$ LHC by using FeynArts 3.5 [22] and CompHEP 4.5.1 [23] packages separately.

ILC	FeynArts [fb]	CompHEP [fb]
$e^+e^- \rightarrow W^+W^-\gamma$	99.15(3)	99.16(2)
$e^+e^- \rightarrow W^+W^-Z$	52.16(2)	52.15(1)
LHC	FeynArts [fb]	CompHEP [fb]
$pp \rightarrow W^+W^-\gamma$	122.84(2)	122.86(3)
$pp \rightarrow W^+W^-Z$	90.35(1)	90.35(1)

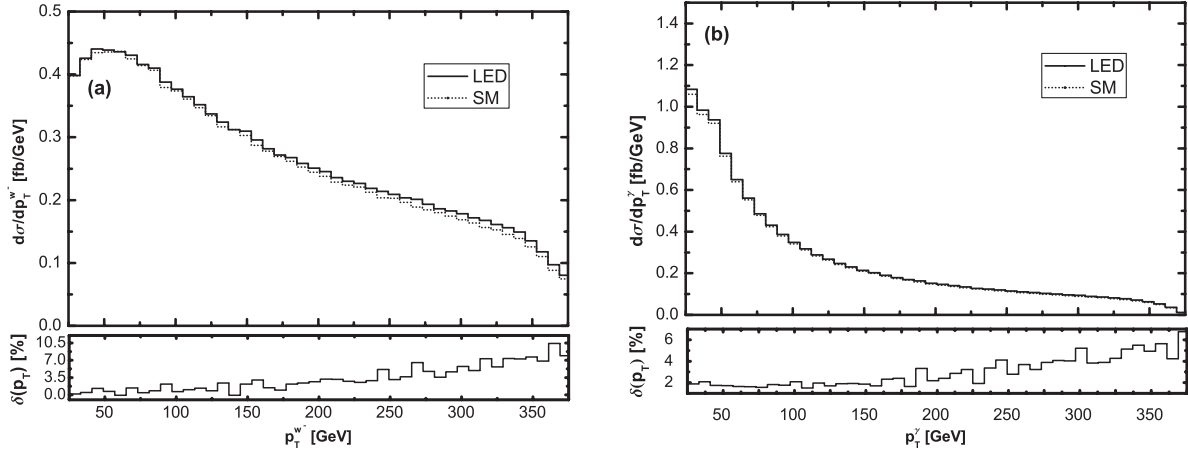


FIG. 4. Transverse momentum and corresponding relative LED discrepancy distributions of final W^- and γ for the $e^+e^- \rightarrow W^+W^-\gamma$ process in both the SM and the LED model at the $\sqrt{s} = 800$ GeV ILC, with the LED parameters $M_S = 3.8$ TeV and $n = 3$. (a) For $p_T^{W^-}$. (b) For p_T^γ .

in Figs. 4 and 5. The $p_T^{W^-}$, p_T^Z , and p_T^γ distributions for the $pp \rightarrow W^+W^-\gamma$, W^+W^-Z processes at the $\sqrt{s} = 14$ TeV LHC are presented in Figs. 6 and 7. In each plot of Figs. 4–7, the $p_T^{W^-}$, p_T^Z , and p_T^γ distributions are provided in both the SM and the LED model for the sake of comparison. We define the relative LED discrepancy of p_T distribution as $\delta(p_T) \equiv (d\sigma_{LED}/dp_T - d\sigma_{SM}/dp_T)/d\sigma_{SM}/dp_T$ to describe the LED effect on the differential cross section, and plot the corresponding $\delta(p_T)$ distribution in the nether plot for each of the figures in Figs. 4–7. All eight figures show that $\delta(p_T^{W^-})$, $\delta(p_T^\gamma)$, and $\delta(p_T^Z)$ at the ILC and LHC become larger with the increment of the transverse momenta. Specifically, in Fig. 4(a) the $\delta(p_T^{W^-})$ lies in the range of 0.7–7.9% for the $e^+e^- \rightarrow W^+W^-\gamma$ process in the region of $25 \text{ GeV} < p_T^{W^-} < 375 \text{ GeV}$, while $\delta(p_T^{W^-})$ varies from 1.7% to 12.0% for the $e^+e^- \rightarrow W^+W^-Z$ process in the same p_T region as shown in Fig. 5(a). From Figs. 4 and 5, one can find that all

the curve behaviors of $\delta(p_T^\gamma)$, $\delta(p_T^Z)$, and $\delta(p_T^{W^-})$ are similar in both the $e^+e^- \rightarrow W^+W^-\gamma$ and $e^+e^- \rightarrow W^+W^-Z$ processes at the ILC. Figures 6 and 7 are for the $pp \rightarrow W^+W^-\gamma$ and $pp \rightarrow W^+W^-Z$ processes at the LHC, respectively. We can see that the LED effects on the $p_T^{W^-}$, p_T^γ , and p_T^Z distributions at the LHC become dominant over the pure SM contributions in the high p_T region. The feature of the p_T distributions at the LHC can serve as LED signal searches in the TGB measurements.

In Figs. 8 and 9, we depict the rapidity (y) distributions of final W pair, γ , and Z boson for the $e^+e^- \rightarrow W^+W^-\gamma$, W^+W^-Z processes at the $\sqrt{s} = 800$ GeV ILC, respectively. Figure 10 shows the y^{WW} and y^γ distributions of the process $pp \rightarrow W^+W^-\gamma$, while Fig. 11 gives the y^{WW} and y^Z distributions for the process $pp \rightarrow W^+W^-Z$. In each plot of Figs. 8–11, there are y^{WW} and y^γ (y^Z) rapidity distributions in both the SM and the LED model, and the

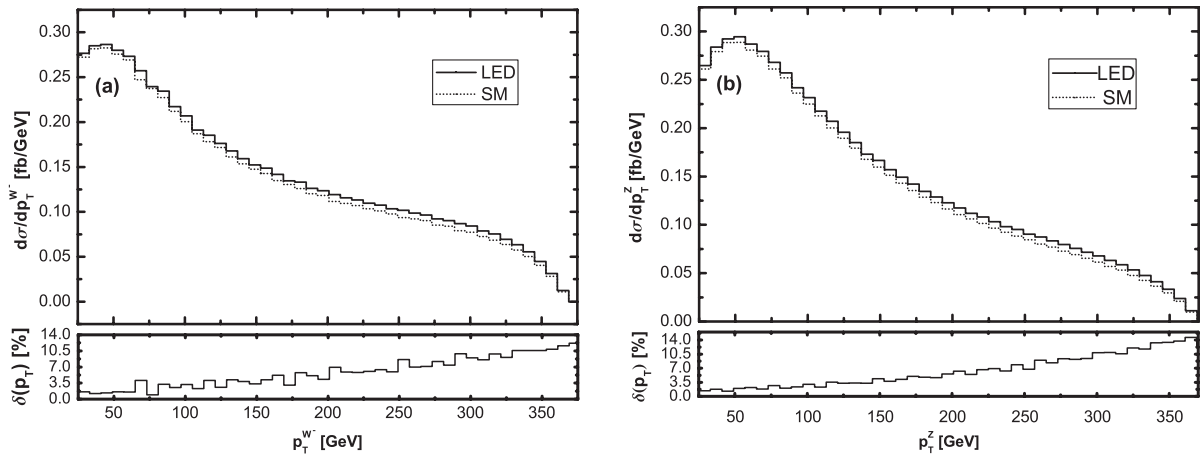


FIG. 5. Transverse momentum and corresponding relative LED discrepancy distributions of final W^- and Z boson for the $e^+e^- \rightarrow W^+W^-Z$ process in both the SM and the LED model at the $\sqrt{s} = 800$ GeV ILC, with the LED parameters $M_S = 3.8$ TeV and $n = 3$. (a) For $p_T^{W^-}$. (b) For p_T^Z .

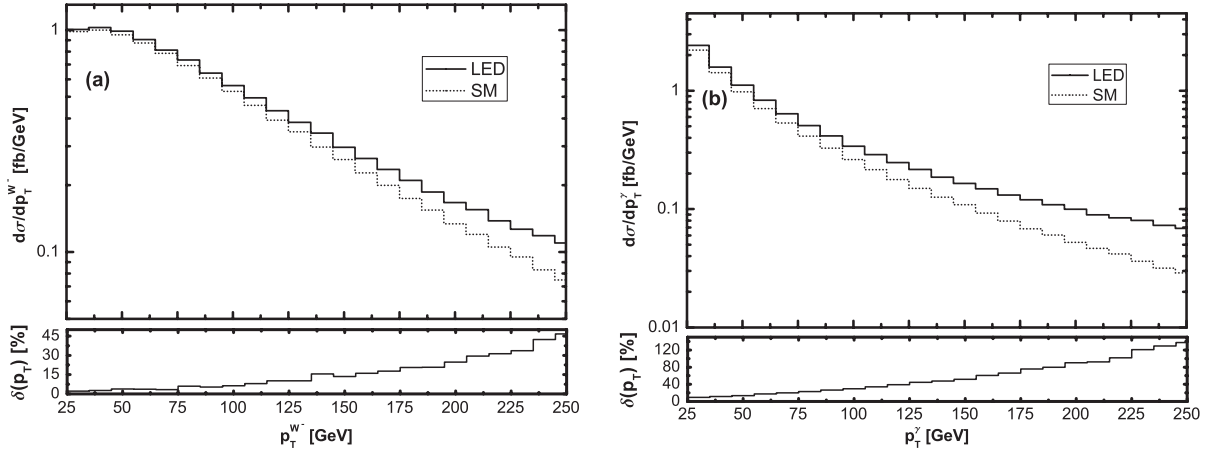


FIG. 6. Transverse momentum and corresponding relative LED discrepancy distributions of final W^- and γ for the $pp \rightarrow W^+W^-\gamma$ process in both the SM and the LED model at the $\sqrt{s} = 14$ TeV LHC, with the LED parameters $M_S = 3.8$ TeV and $n = 3$. (a) For $p_T^{W^-}$. (b) For p_T^γ .

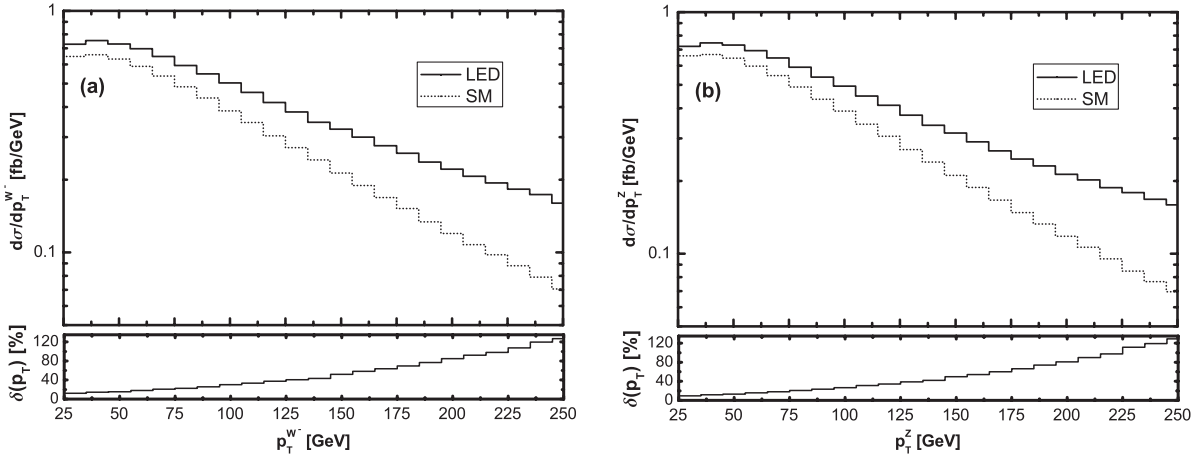


FIG. 7. Transverse momentum and corresponding relative LED discrepancy distributions of final W^- and Z boson for the $pp \rightarrow W^+W^-Z$ process in both the SM and the LED model at the $\sqrt{s} = 14$ TeV LHC, with the LED parameters $M_S = 3.8$ TeV and $n = 3$. (a) For $p_T^{W^-}$. (b) For p_T^Z .

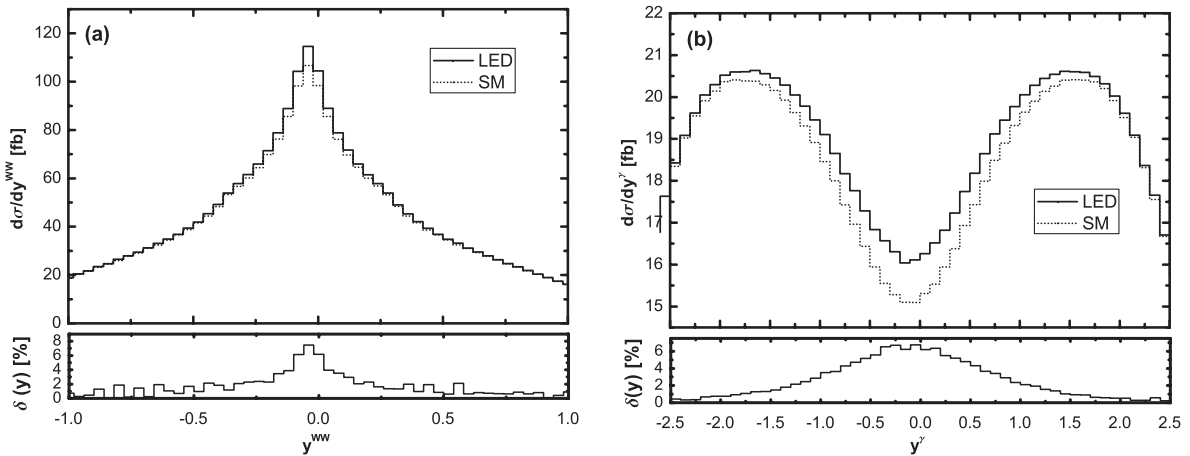


FIG. 8. Rapidity and corresponding relative LED discrepancy distributions of final W pair and γ for the $e^+e^- \rightarrow W^+W^-\gamma$ process in both the SM and the LED model at the $\sqrt{s} = 800$ GeV ILC, with the LED parameters $M_S = 3.8$ TeV and $n = 3$. (a) For y^{WW} . (b) For y^γ .

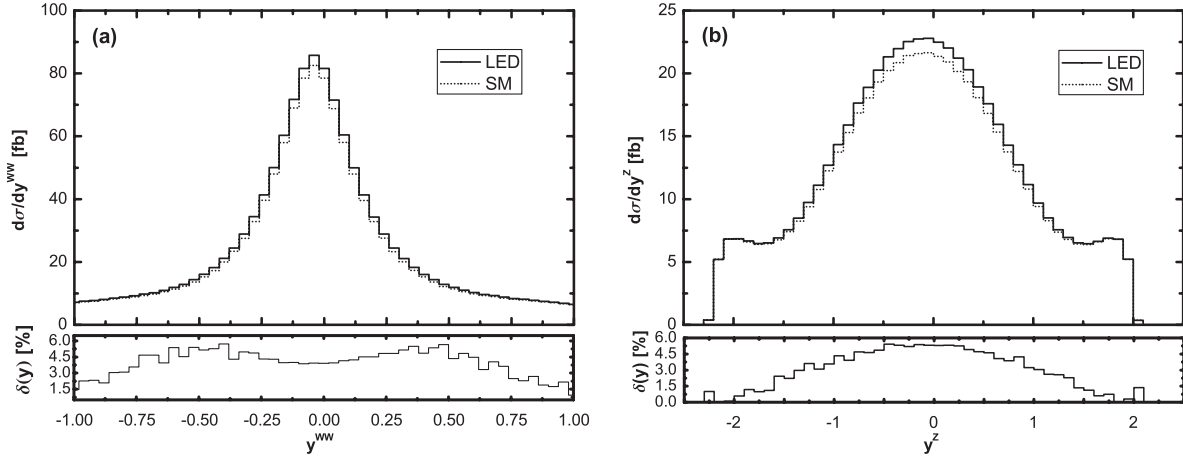


FIG. 9. Rapidity and corresponding relative LED discrepancy distributions of final W pair and Z boson for the $e^+e^- \rightarrow W^+W^-Z$ process in both the SM and the LED model at the $\sqrt{s} = 800$ GeV ILC, with the LED parameters $M_S = 3.8$ TeV and $n = 3$. (a) For y^{WW} . (b) For y^Z .

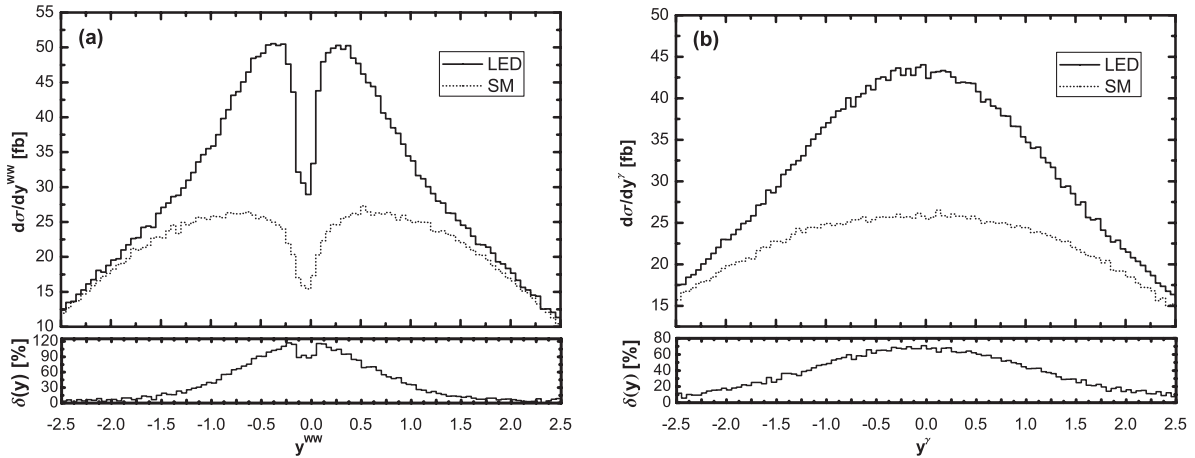


FIG. 10. Rapidity and corresponding relative LED discrepancy distributions of final W pair and γ for the $pp \rightarrow W^+W^-\gamma$ process in both the SM and the LED model at the $\sqrt{s} = 14$ TeV LHC, with the LED parameters $M_S = 3.8$ TeV and $n = 3$. (a) For y^{WW} . (b) For y^γ .

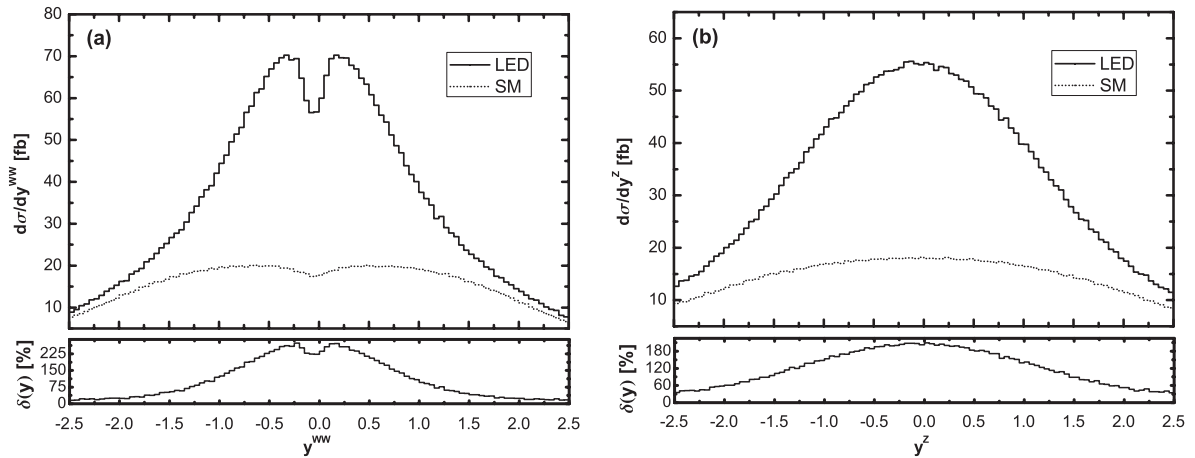


FIG. 11. Rapidity and corresponding relative LED discrepancy distributions of final W pair and Z boson for the $pp \rightarrow W^+W^-Z$ process in both the SM and the LED model at the $\sqrt{s} = 14$ TeV LHC, with the LED parameters $M_S = 3.8$ TeV and $n = 3$. (a) For y^{WW} . (b) For y^Z .

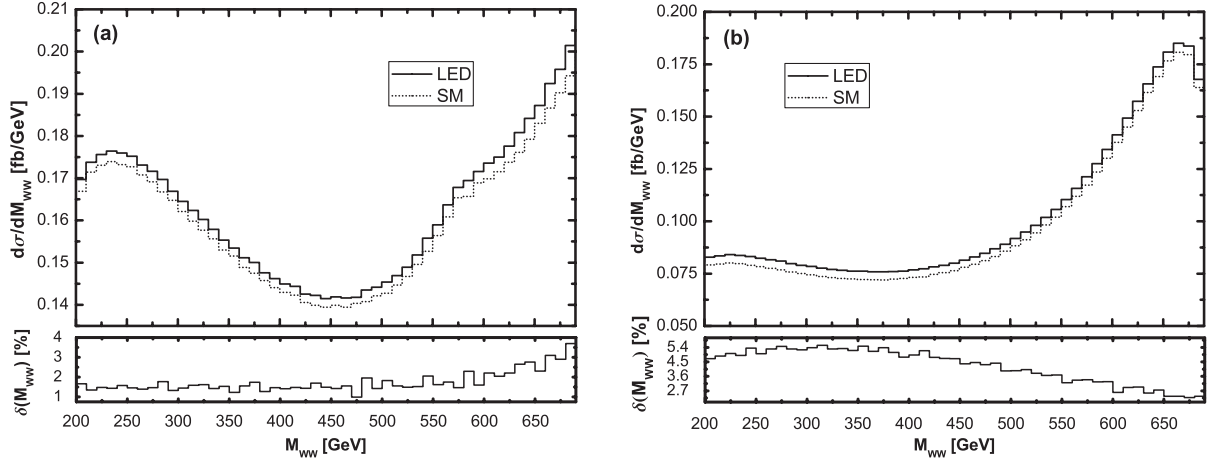


FIG. 12. M_{WW} and corresponding relative LED discrepancy distributions in both the SM and the LED model at the $\sqrt{s} = 800$ GeV ILC, with the LED parameters $M_S = 3.8$ TeV and $n = 3$. (a) For the $e^+e^- \rightarrow W^+W^-\gamma$ process. (b) For the $e^+e^- \rightarrow W^+W^-Z$ process.

corresponding relative LED discrepancy $\delta(y)$ distribution, where we define $\delta(y) \equiv (\frac{d\sigma_{LED}}{dy} - \frac{d\sigma_{SM}}{dy}) / \frac{d\sigma_{SM}}{dy}$. We can see from all the figures that the contributions from the LED manifest themselves obviously in the central rapidity regions at both colliders. From Figs. 8(b), 9(b), 10(b), and 11(b), we see that the relative LED discrepancies, $\delta(y^\gamma)$ and $\delta(y^Z)$, respectively reach their peaks at the locations of $y^{\gamma(Z)} \sim 0$ with maximum values about 6% at the ILC and beyond 50% (140%) for y^γ (y^Z) at the LHC.

Figures 12 and 13 show the W -pair invariant mass (M_{WW}) distributions in both the SM and the LED model at the ILC and LHC, respectively. Their corresponding relative LED discrepancies ($\delta(M_{WW}) \equiv (\frac{d\sigma_{LED}}{dM_{WW}} - \frac{d\sigma_{SM}}{dM_{WW}}) / \frac{d\sigma_{SM}}{dM_{WW}}$) are also illustrated there. Figure 12(a) shows that $\delta(M_{WW})$ for the $e^+e^- \rightarrow W^+W^-\gamma$ process increases when M_{WW} goes up in the plotted range, and reaches its maximum of about 3.7% at the position of $M_{WW} = 690$ GeV.

In contrast, we can see from Fig. 12(b) that $\delta(M_{WW})$ for the $e^+e^- \rightarrow W^+W^-Z$ process rises gradually until it reaches the maximal value of about 5.5% at the position of $M_{WW} = 320$ GeV, and then decreases with the increment of M_{WW} . In Fig. 13, the M_{WW} distributions for the two processes $pp \rightarrow W^+W^-\gamma$ and $pp \rightarrow W^+W^-Z$ demonstrate the similar behavior; it shows that the LED effect is going to be dominant with the increment of invariant mass of the W pair at the LHC.

In Figs. 14 and 15, we give the integrated cross section and the corresponding relative LED discrepancy, defined as $\delta(\sqrt{s}) \equiv \frac{\sigma_{LED} - \sigma_{SM}}{\sigma_{SM}}$, as functions of the c.m.s. energy \sqrt{s} at the ILC and LHC, respectively. From Fig. 14(a), we see that the distribution of the cross section for the $e^+e^- \rightarrow W^+W^-\gamma$ process decreases with the increment of \sqrt{s} , while in Fig. 14(b) it shows that the distribution for the $e^+e^- \rightarrow W^+W^-Z$ process behaves in the opposite way. In Fig. 15, the cross sections for the $pp \rightarrow W^+W^-\gamma$, W^+W^-Z processes rise sharply when \sqrt{s} goes up, and the relative LED

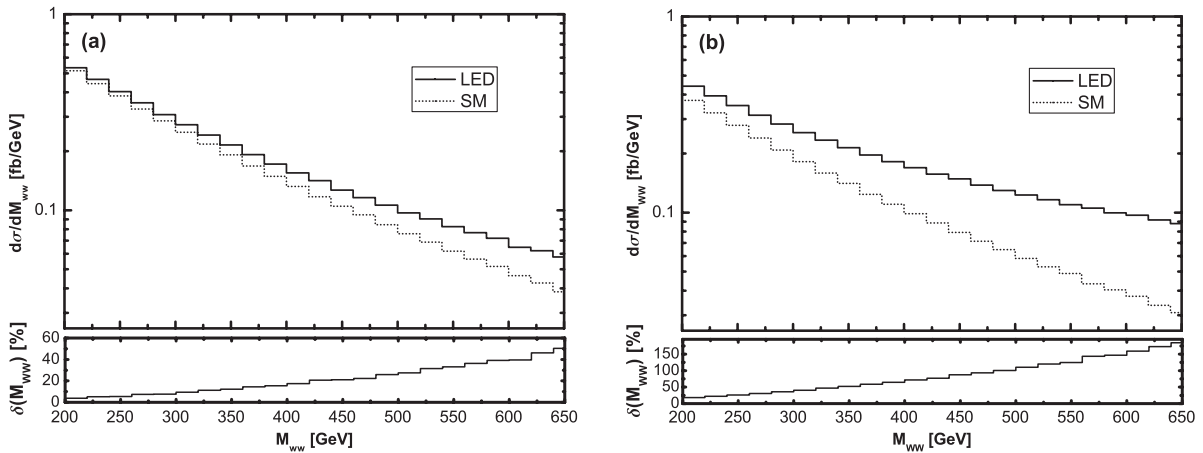


FIG. 13. M_{WW} and corresponding relative LED discrepancy distributions in both the SM and the LED model at the $\sqrt{s} = 14$ TeV LHC, with the LED parameters $M_S = 3.8$ TeV and $n = 3$. (a) For the $pp \rightarrow W^+W^-\gamma$ process. (b) For the $pp \rightarrow W^+W^-Z$ process.

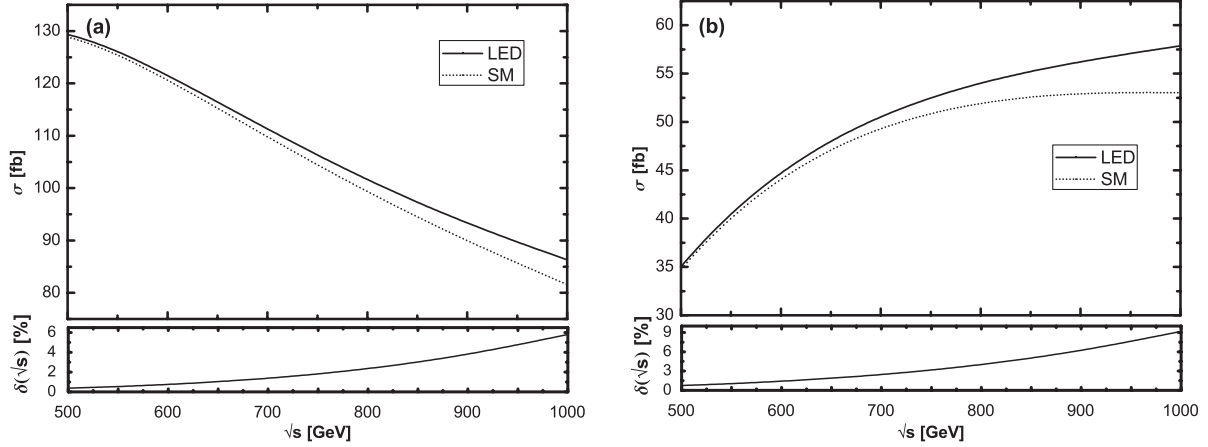


FIG. 14. The integrated cross section and the corresponding relative LED discrepancy as the functions of the c.m.s. energy \sqrt{s} in both the SM and the LED model at the ILC, with \sqrt{s} varying from 500 GeV to 1 TeV, the LED parameters $M_S = 3.8$ TeV, and $n = 3$. (a) For the $e^+e^- \rightarrow W^+W^-\gamma$ process. (b) For the $e^+e^- \rightarrow W^+W^-Z$ process.

discrepancies $\delta(\sqrt{s})$ at the LHC are quantitatively almost one order larger than those at the ILC.

All the figures above show that there exists a remarkable enhancement of the relative LED discrepancy at the LHC in comparison with that at the ILC. This can be ascribed to the following two reasons: (1) Unlike the $pp \rightarrow W^+W^-\gamma/Z$ process in the SM, this process in the LED model arises from not only the $q\bar{q}$ annihilations, but also the additional gg fusion subprocess. In addition, the large gluon luminosity at the LHC can further enhance the LED effect. (2) Since the continuous large colliding energy ($\sqrt{\hat{s}}$) spectrum available at the LHC can be in the range not far away from the cutoff scale Λ taken to be M_S , the resonant contribution of the single KK-graviton mode in the s channel will be included.

In Tables II and III, we list the values of the integrated cross sections in the SM and the LED model for the

$e^+e^- \rightarrow W^+W^-\gamma/Z$ and the $pp \rightarrow W^+W^-\gamma/Z$ processes with some typical colliding energies at the ILC and LHC, separately. In Table III, we give additionally the cross section contributions from the $pp \rightarrow gg \rightarrow W^+W^-\gamma, W^+W^-Z$ processes. Comparing the results in Tables II and III, we can see that in the pp collision case the existence of the additional gg fusion partonic process and the KK-graviton resonance effect induced by the large colliding energy spectrum obviously enhance the SM cross section.

In Figs. 16 and 17, we present the integrated cross sections as functions of M_S with different numbers of extra dimensions n for the $W^+W^-\gamma/Z$ production processes at the ILC and LHC, respectively. The horizon line in each figure corresponds to the SM cross section which is independent of the LED parameters M_S and n . It can be found that the deviations due to the LED contributions from the

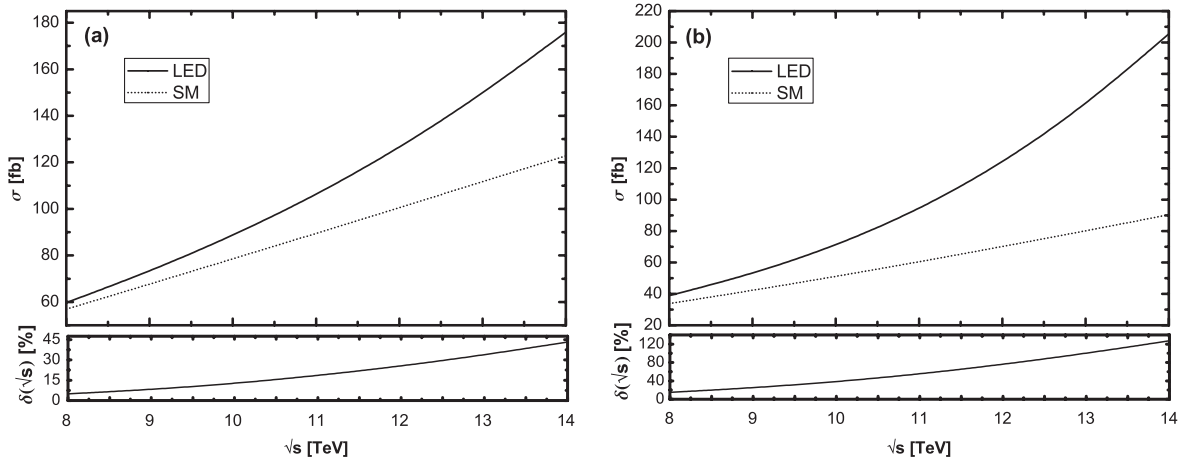


FIG. 15. The integrated cross section and the corresponding relative LED discrepancy as the functions of the c.m.s. energy \sqrt{s} in both the SM and the LED model at the LHC, with \sqrt{s} varying from 8 to 14 TeV, the LED parameters $M_S = 3.8$ TeV, and $n = 3$. (a) For the $pp \rightarrow W^+W^-\gamma$ process. (b) For the $pp \rightarrow W^+W^-Z$ process.

TABLE II. The integrated cross sections for the $e^+e^- \rightarrow W^+W^-\gamma$ and $e^+e^- \rightarrow W^+W^-Z$ processes in both the SM and the LED model at the ILC, with the LED parameters $M_S = 3.8$ TeV, $n = 3$, and \sqrt{s} varying from 500 GeV to 1 TeV.

\sqrt{s} [GeV]	$e^+e^- \rightarrow W^+W^-\gamma$		$e^+e^- \rightarrow W^+W^-Z$	
	σ_{SM} [fb]	σ_{LED} [fb]	σ_{SM} [fb]	σ_{LED} [fb]
500	130.36(3)	130.82(3)	35.70(1)	35.96(1)
600	120.87(3)	121.74(3)	44.71(1)	45.33(1)
700	109.71(3)	111.16(3)	49.70(1)	50.89(1)
800	99.15(2)	101.41(3)	52.16(1)	54.20(1)
900	89.76(2)	93.10(2)	53.07(1)	56.30(2)
1000	81.58(2)	86.30(2)	53.01(1)	57.86(2)

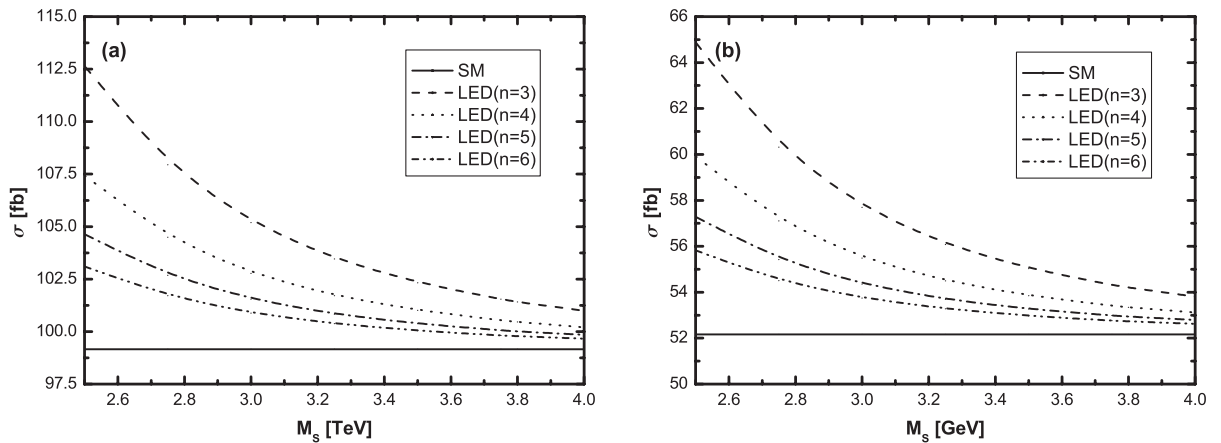
TABLE III. The integrated cross sections for the $pp \rightarrow W^+W^-\gamma$ and the $pp \rightarrow W^+W^-Z$ processes in both the SM and the LED model at the LHC, with the LED parameters $M_S = 3.8$ TeV, $n = 3$, and \sqrt{s} varying from 8 to 14 TeV, where the $\sigma_{\text{LED}}(\text{total})$ is the integrated cross section via both $q\bar{q}$ annihilation and gg fusion, while $\sigma_{\text{LED}}(gg)$ denotes the integrated cross section only via gg fusion.

\sqrt{s} [TeV]	$pp \rightarrow W^+W^-\gamma$			$pp \rightarrow W^+W^-Z$		
	σ_{SM} [fb]	$\sigma_{\text{LED}}(\text{total})$ [fb]	$\sigma_{\text{LED}}(gg)$ [fb]	σ_{SM} [fb]	$\sigma_{\text{LED}}(\text{total})$ [fb]	$\sigma_{\text{LED}}(gg)$ [fb]
8	56.92(1)	59.74(1)	0.45(1)	33.83(1)	38.92(1)	1.27(2)
9	67.64(1)	73.14(1)	1.06(1)	44.22(1)	52.61(1)	3.00(3)
10	78.52(1)	88.41(1)	2.21(2)	51.10(1)	70.45(1)	6.28(4)
11	89.50(1)	105.92(1)	4.20(3)	60.40(1)	93.56(1)	11.91(5)
12	100.56(2)	126.14(2)	7.30(5)	70.06(1)	123.07(1)	20.81(7)
13	111.69(2)	149.38(2)	11.87(6)	80.05(1)	160.05(2)	33.94(1)
14	122.84(2)	175.96(2)	18.25(7)	90.35(1)	205.55(3)	52.35(2)

SM predictions become more distinct when n is small. On the other hand, for a fixed value of n , the integrated cross section decreases with the increment of M_S and gradually approaches to the SM prediction. These features of the relationship between the integrated cross section and the LED parameters M_S and n are manifested in the $W^+W^-\gamma/Z$ production processes at both the ILC and LHC, which can be seen in Figs. 16 and 17, respectively.

From the above analysis, we see that the LED effects can generally enhance the kinematic observables, especially at the LHC. To further explore the discovery and exclusion potential for the LED signals at the ILC and LHC, we adopt the 5σ discovery limit and 3σ exclusion limit to study the constraints on the fundamental scale M_S , namely,

$$\Delta\sigma = \sigma_{\text{LED}} - \sigma_{\text{SM}} \geq \frac{5\sqrt{\mathcal{L}\sigma_{\text{LED}}}}{\mathcal{L}} \equiv 5\sigma, \quad (4.2)$$

FIG. 16. The integrated cross sections as functions of M_S with n varying from 3 to 6 at the $\sqrt{s} = 800$ GeV ILC. The SM results appear as the straight lines. (a) For the $e^+e^- \rightarrow W^+W^-\gamma$ process. (b) For the $e^+e^- \rightarrow W^+W^-Z$ process.

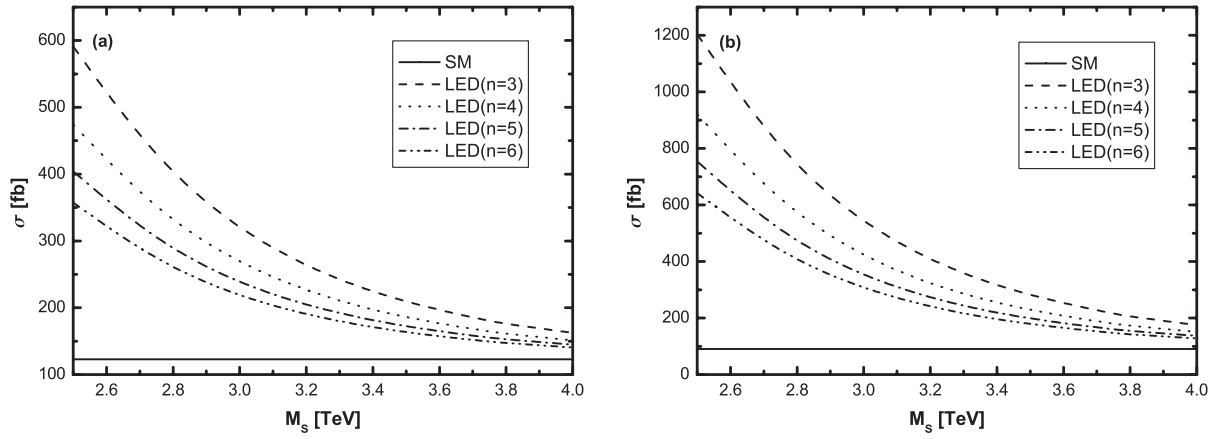


FIG. 17. The integrated cross sections as functions of M_S with n varying from 3 to 6 at the $\sqrt{s} = 14$ TeV LHC. The SM results appear as the straight lines. (a) For the $pp \rightarrow W^+W^-\gamma$ process. (b) For the $pp \rightarrow W^+W^-Z$ process.

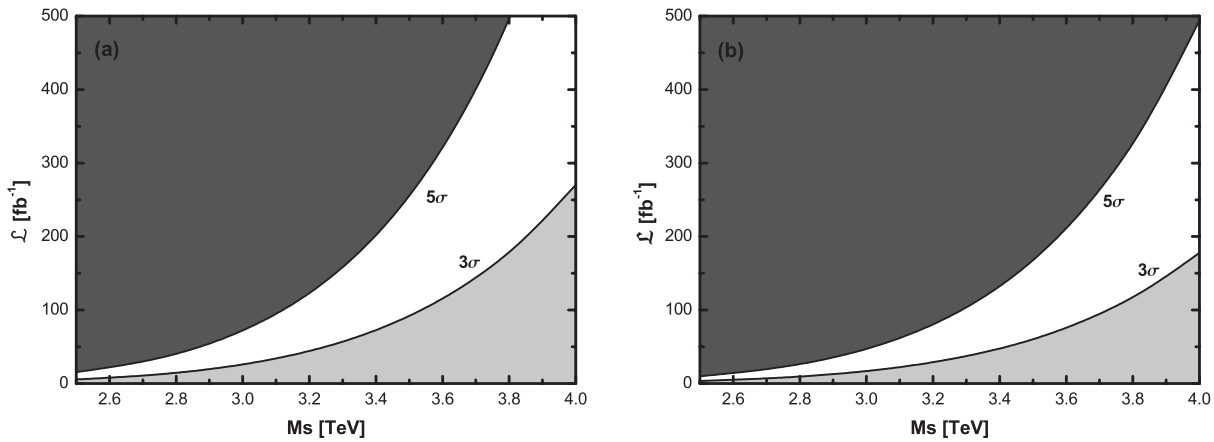


FIG. 18. The LED effect discovery area (dark) and exclusion area (gray) in the $\mathcal{L} - M_S$ space at the $\sqrt{s} = 800$ GeV ILC, where $n = 3$. (a) For the $e^+e^- \rightarrow W^+W^-\gamma$ process. (b) For the $e^+e^- \rightarrow W^+W^-Z$ process.

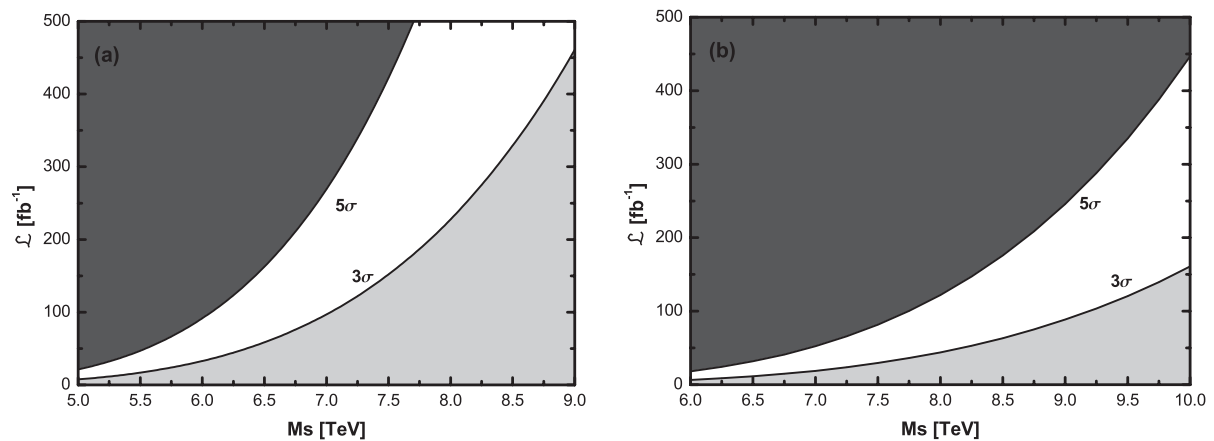


FIG. 19. The LED effect discovery area (dark) and exclusion area (gray) in the $\mathcal{L} - M_S$ space at the $\sqrt{s} = 14$ TeV LHC, where $n = 3$. (a) For the $pp \rightarrow W^+W^-\gamma$ process. (b) For the $pp \rightarrow W^+W^-Z$ process.

TABLE IV. The discovery ($\Delta\sigma \geq 5\sigma$) and exclusion ($\Delta\sigma \leq 3\sigma$) limits on the fundamental scale M_S for the $e^+e^- \rightarrow W^+W^-\gamma$ and $e^+e^- \rightarrow W^+W^-Z$ processes at the $\sqrt{s} = 800$ GeV ILC, where $n = 3$.

Luminosity (\mathcal{L}) [fb^{-1}]	$e^+e^- \rightarrow W^+W^-\gamma$		$e^+e^- \rightarrow W^+W^-Z$	
	M_S [TeV] (3σ)	M_S [TeV] (5σ)	M_S [TeV] (3σ)	M_S [TeV] (5σ)
50	3.25	2.87	3.42	3.02
100	3.54	3.12	3.72	3.29
150	3.73	3.28	3.91	3.45

TABLE V. The discovery ($\Delta\sigma \geq 5\sigma$) and exclusion ($\Delta\sigma \leq 3\sigma$) limits on the fundamental scale M_S for the $pp \rightarrow W^+W^-\gamma$ and $pp \rightarrow W^+W^-Z$ processes at the $\sqrt{s} = 14$ TeV LHC, where $n = 3$.

Luminosity(\mathcal{L}) [fb^{-1}]	$pp \rightarrow W^+W^-\gamma$		$pp \rightarrow W^+W^-Z$	
	M_S [TeV] (3σ)	M_S [TeV] (5σ)	M_S [TeV] (3σ)	M_S [TeV] (5σ)
50	6.35	5.54	8.18	6.92
100	7.04	6.07	9.20	7.75
150	7.48	6.42	9.87	8.28

$$\Delta\sigma = \sigma_{\text{LED}} - \sigma_{\text{SM}} \leq \frac{3\sqrt{\mathcal{L}\sigma_{\text{LED}}}}{\mathcal{L}} \equiv 3\sigma. \quad (4.3)$$

In Figs. 18(a) and 18(b), we present the discovery and exclusion regions in the $\mathcal{L} - M_S$ space for the $e^+e^- \rightarrow W^+W^-\gamma$ and $e^+e^- \rightarrow W^+W^-Z$ processes at the $\sqrt{s} = 800$ GeV ILC with $n = 3$, separately. In Figs. 19(a) and 19(b), the discovery and exclusion regions for the $pp \rightarrow W^+W^-\gamma$ and $pp \rightarrow W^+W^-Z$ processes at the $\sqrt{s} = 14$ TeV LHC with $n = 3$ are given, respectively. The dark and gray regions in Figs. 18 and 19 represent the $\mathcal{L} - M_S$ space with the 5σ discovery limit and 3σ exclusion limit, separately. Some typical limits for M_S with the integrated luminosity $\mathcal{L} = 50, 100, 150 \text{ fb}^{-1}$, which are read out from Figs. 18 and 19, are listed in Tables IV and V, separately. It is found that the values of the 5σ discovery and 3σ exclusion limits on M_S at the LHC are larger than those obtained at the ILC with the same integrated luminosity. This reflects the fact that the $W^+W^-\gamma/Z$ production rates at the LHC are enhanced by the additional gg fusion subprocess and the KK-graviton resonant effect induced by the available large colliding energy, and this feature can further be viewed as the advantage of the LHC over the ILC in exploring the LED signature from the $W^+W^-\gamma/Z$ production measurements [16].

V. SUMMARY

In this paper, we study the LED effects induced by the virtual KK graviton on the $W^+W^-\gamma$ and W^+W^-Z production processes at both the LHC and ILC. The comparison

between the results for these productions at both colliders are made. We present the transverse momentum and rapidity distributions of final particles, and find that the LED contributions remarkably affect the observables of these processes, particularly in either the high transverse momentum region or the central rapidity region ($y \sim 0$). We see that the relative LED discrepancy becomes larger with the increment of the invariant mass of final W pair, and the integrated cross section in the LED model decreases when M_S goes up for a fixed n at both the ILC and LHC. The 5σ discovery and 3σ exclusion limits on the fundamental scale M_S are also obtained at both the ILC and LHC. We also find that the relative LED discrepancy for the $W^+W^-\gamma/Z$ production at the LHC is generally larger than that at the ILC due to the additional LED contributions via gg fusion subprocesses and the KK-graviton exchanging resonant effect induced by the continuous large colliding energy available in the LHC. From the aspect of effectively exploring the LED signal in measuring $W^+W^-\gamma/Z$ production, we conclude that the $W^+W^-\gamma$ and W^+W^-Z productions at the LHC could have the distinct advantage over at the ILC.

ACKNOWLEDGMENTS

This work was supported in part by the National Natural Science Foundation of China (Grants No. 11075150 and No. 11005101), and the Specialized Research Fund for the Doctoral Program of Higher Education (Grant No. 20093402110030).

- [1] G. Weiglein *et al.* (LHC/LC Study Group Collaboration), *Phys. Rep.* **426**, 47 (2006).
- [2] N. Arkani-Hamed, S. Dimopoulos, and G. Dvali, *Phys. Lett. B* **429**, 263 (1998); *Phys. Rev. D* **59**, 086004 (1999); I. Antoniadis, N. Arkani-Hamed, S. Dimopoulos, and G. Dvali, *Phys. Lett. B* **436**, 257 (1998).
- [3] K. Agashe and N.G. Deshpande, *Phys. Lett. B* **456**, 60 (1999).
- [4] N. Agarwal, V. Ravindran, V.K. Tiwari, and A. Tripathi, *Nucl. Phys.* **B830**, 248 (2010); *Phys. Rev. D* **82**, 036001 (2010); M.C. Kumar, P. Mathews, V. Ravindran, and A. Tripathi, *Phys. Lett. B* **672**, 45 (2009).
- [5] S. Ask, *Eur. Phys. J. C* **60**, 509 (2009); X.D. Gao, C.S. Li, J. Gao, and J. Wang, *Phys. Rev. D* **81**, 036008 (2010); M.C. Kumar, P. Mathews, V. Ravindran, and S. Seth, *Nucl. Phys.* **B847**, 54 (2011).
- [6] Y. -M. Bai, L. Guo, X. -Z. Li, W. -G. Ma, and R. -Y. Zhang, *Phys. Rev. D* **85**, 016008 (2012).
- [7] S. Karg, M. Kramer, Q. Li, and D. Zeppenfeld, *Phys. Rev. D* **81**, 094036 (2010).
- [8] S. Godfrey, *AIP Conf. Proc.* **350**, 209 (1995); O.J.P. Eboli, M.C. Gonzalez-Garcia, and S.M. Lietti, *Phys. Rev. D* **69**, 095005 (2004).
- [9] F. Ferro *et al.*, [arXiv:1012.5169](https://arxiv.org/abs/1012.5169).
- [10] A. Lazopoulos, K. Melnikov, and F. Petriello, *Phys. Rev. D* **76**, 014001 (2007); V. Hankele and D. Zeppenfeld, *Phys. Lett. B* **661**, 103 (2008); G. Bozzi, F. Campanario, V. Hankele, and D. Zeppenfeld, *Phys. Rev. D* **81**, 094030 (2010).
- [11] M.C. Kumar, P. Mathews, V. Ravindran, and S. Seth, *Phys. Rev. D* **85**, 094507 (2012).
- [12] ALEPH, DELPHI, L3, OPAL Collaborations, and LEP Electroweak Working Group, Report No. CERN-PH-EP/2005-051 (unpublished); L3 Collaboration, *Phys. Lett. B* **490**, 187 (2000).
- [13] O.J.P. Eboli, M.C. Gonzalez-Garcia, S.M. Lietti, and S.F. Novaes, *Phys. Rev. D* **63**, 075008 (2001); D. Green, [arXiv:hep-ex/0310004](https://arxiv.org/abs/hep-ex/0310004).
- [14] J. Reuter, *LCWS/ILC, DESY, Hamburg, 2007*, eConf C0705302, TEV04 (2007); H. Yamamoto, *J. Phys. Soc. Jpn.* **76**, 111014 (2007).
- [15] T. Han, J.D. Lykken, and R. -J. Zhang, *Phys. Rev. D* **59**, 105006 (1999).
- [16] G.F. Giudice, R. Rattazzi, and J.D. Wells, *Nucl. Phys.* **B544**, 3 (1999).
- [17] J. Pumplin, D.R. Stump, J. Huston, H.L. Lai, P.M. Nadolsky, and W.K. Tung, *J. High Energy Phys.* **07** (2002) 012.
- [18] J. Beringer *et al.* (Particle Data Group), *Phys. Rev. D* **86**, 010001 (2012).
- [19] G. Aad *et al.* (ATLAS Collaboration), *Phys. Lett. B* **710**, 538 (2012).
- [20] CMS Collaboration, Report No. CMS-EXO-11-038 and CERN-PH-EP-2011-173 (unpublished).
- [21] S. Chatrchyan *et al.* (CMS Collaboration), *Phys. Lett. B* **711**, 15 (2012).
- [22] T. Hahn, *Comput. Phys. Commun.* **140**, 418 (2001).
- [23] E. Boos *et al.*, Proc. Sci., ACAT08 (2009) 008 [[arXiv:0901.4757](https://arxiv.org/abs/0901.4757)].